Geophysical Prospecting

EAGE EUROPEAN ASSOCIATION OF GEOSCIENTISTS & ENGINEERS

Geophysical Prospecting doi: 10.1111/1365-2478.12095

Tube wave to shear wave conversion at borehole plugs

Tim Seher[1]*, Stephane Rondenay[2] and Hugues Djikpesse[3,4]

[1]*Formerly at: Earth Resources Laboratory, Massachusetts Institute of Technology, 77 Massachusetts Avenue, Cambridge, MA 02139-4307, U.S.A.,* [2]*University of Bergen – Department of Earth Science, Bergen, Norway,* [3]*Schlumberger-Doll Research, Cambridge, Massachusetts, United States, and* [4]*Visiting Scientist, Energy Initiatives, Massachusets Institute of Technology, Cambridge, MA, U.S.A.*

Received September 2012, revision accepted June 2013

ABSTRACT

In hydraulic fracturing experiments, perforation shots excite body and tube waves that sample, and thus can be used to characterize, the surrounding medium. While these waves are routinely employed in borehole operations, their resolving power is limited by the experiment geometry, the signal-to-noise ratio, and their frequency content. It is therefore useful to look for additional, complementary signals that could increase this resolving power. Tube-to-body-wave conversions (scattering of tube to compressional or shear waves at borehole discontinuities) are one such signal. These waves are not frequently considered in hydraulic fracture settings, yet they possess geometrical and spectral attributes that greatly complement the resolution afforded by body and tube waves alone. Here, we analyze data from the Jonah gas field (Wyoming, USA) to demonstrate that tube-to-shear-wave conversions can be clearly observed in the context of hydraulic fracturing experiments. These waves are identified primarily on the vertical and radial components of geophones installed in monitoring wells surrounding a treatment well. They exhibit a significantly lower frequency content (10–100 Hz) than the primary compressional waves (100–1000 Hz). Tapping into such lower frequencies could help to better constrain velocity in the formation, thus allowing better estimates of fracture density, porosity and permeability. Moreover, the signals of tube-to-shear-wave conversion observed in this particular study provide independent estimates of the shear wave velocity in the formation and of the tube wave velocity in the treatment well.

Key words: Seismics, Wave, Borehole geophysics, Monitoring.

1 INTRODUCTION

Traditionally, exploration seismologists have mainly used reflected and refracted seismic body waves for subsurface characterization. However, an increase in seismic borehole experiments and improved instrumentation have allowed the observation of other useful, albeit less common waves (Fig. 1a). These include conversions from tube to shear waves – the focus of this study – which provide additional resolving power that can advance the understanding of the subsurface.

Tube waves, which propagate along the borehole, may emanate from seismic sources located inside the borehole. Whenever there are obstacles within the borehole, tube waves may be converted to body waves (either compressional or shear waves). Such conversions have been observed in situations where a tube wave reaches the bottom of the borehole, or where a tube wave impinges upon open fractures or irregularities in the borehole wall (White and Sengbush 1963; Lee *et al.* 1984; Beydoun *et al.* 1985; Hardage 2000; Greenhalgh *et al.* 2000, 2003; Xu and Greenhalgh 2010). In particular, tube-to-body-wave conversions have been exploited as secondary sources for borehole seismic experiments (Norris and Aronstam 2003; Aronstam 2004). Similar reciprocal conversions from body to tube wave may occur when a body wave passes through a borehole.

*E-mail: tseher@web.de

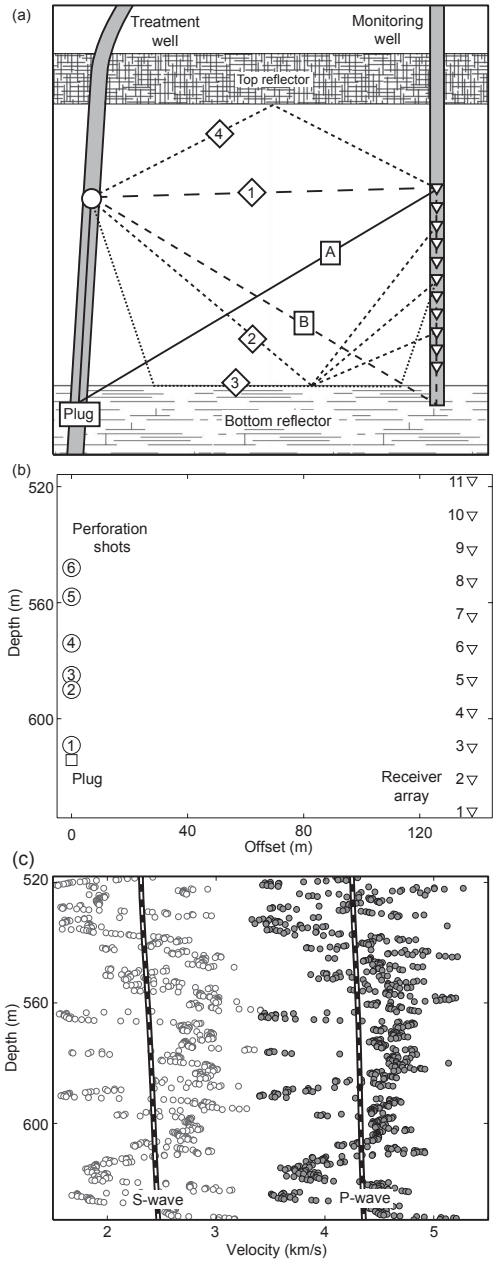

Figure 1 (a) Illustration of different seismic raypath. (1) Direct compressional (P) and shear (S) waves. (2) PP, PS, SP and SS reflections from a bottom reflector. (3) Critically refracted waves. (4) Reflections from a top reflector. (A) Diffraction at a plug in the treatment well. (B) Diffraction at the bottom of the receiver or source well. (b) Experiment geometry to scale. The circles mark the locations of explosive charges, the triangles the receiver locations, and the square the location of the borehole plug. (c) Seismic velocities measured in a nearby borehole. The gray and white circles mark the P-wave and S-wave velocity measurements, respectively. The solid lines mark the moving average of the measurements.

Receivers located either at the surface or within a nearby borehole may detect these converted tube waves. However, tube-to-body-wave conversions are not the only sources of secondary arrivals. Apart from direct waves, reflections and head waves, other borehole-specific events have been observed. For example, Wills *et al.* (1992) describe conical wave observations. These occur when the borehole velocity is greater than the velocity of the surrounding medium, such that seismic waves propagating along the borehole axis give rise to continuous shear wave emissions into that surrounding medium. In another example, Albright and Johnson (1990) describe the partial conversion of Stoneley waves to channel waves in a coal layer intersecting the borehole axis.

Various studies have identified secondary arrivals in seismic borehole experiments. However, tube-to-body-wave conversions have not yet been investigated in hydraulic fracture settings, where such conversions occur in response to standard well operations. During the first stage of a hydraulic fracture experiment, a portion of the treatment well is closed off using borehole plugs. The borehole wall is then broken using multiple explosive sources, which are referred to as perforation shots. These perforation shots may create tube waves, which would then be converted to compressional or shear waves at the borehole plugs, and may be observable by remote seismic receivers. However, such tube-to-body-wave conversions have not been commonly observed or systematically analyzed in the context of hydraulic fracture monitoring.

A better understanding and characterization of these converted waves in a hydraulic fracture setting is valuable for a range of reasons. First, it will allow us to formally identify tube-to-body-wave conversions in a setting where they have not been extensively studied until now. Second, the converted waves carry information about the tube wave velocity between the source and the conversion point, and about the body wave velocity between the conversion point and the receiver. While the body wave velocity is determined by the elastic properties of the medium surrounding the borehole, the tube wave velocity depends on the velocity of both the borehole fluid and the borehole wall. Third, converted waves may help to refine the parameters of the hydraulic fracture experiment (i.e., velocity; source location and properties; receiver location, coupling and orientation), which may allow the improvement of the hydraulic fracturing process. Fourth, the use of tube-to-body-wave conversions allows an increase in resolution both through increased ray coverage and increased spectral content.

This study analyzes perforation shots triggered during a hydraulic fracture experiment in the Jonah gas field,

situated in the Rocky Mountains region of Wyoming – one of the largest onshore natural gas discoveries in the United States (Robinson and Shanley 2005). The focus of this article is on the observation of tube-to-body wave conversions. Therefore, the methodology used to test for the origin of the observed signal is detailed in appendices A, B, and C. In the next section, we concentrate on the validation and physical interpretation of this observation. The seismograms associated with the perforation shots exhibit strong secondary seismic arrivals. Here, we explore different explanations for those arrivals and demonstrate that the most likely explanation is tube-to-shear-wave scattering at plugs in the treatment well. Based on this result, we derive a simple method for calibrating the tube wave velocity in the treatment well that provides new insights in the low frequency behaviour of tube waves. We conclude by discussing the properties and possible future uses of the tube-to-shear-wave scattered signal.

2 OBSERVATIONS AND ANALYSIS

The seismic wave created by a single source usually contains information beyond compressional and shear wave arrivals, which is rarely exploited completely. This is often linked to difficulties in assigning parts of the seismic coda to a unique origin. However, if a part of the seismic coda has been successfully identified, it usually advances the understanding of the subsurface. Here, we commence our analysis by presenting observations of both primary and secondary arrivals. Then we investigate a range of possible mechanisms to explain the origin of the secondary arrivals, and use independent observations from microearthquakes to validate our choice of preferred mechanism.

2.1 Observations from perforation shots

We examine the seismograms created by perforation shots detonated during one stage of a hydraulic fracture experiment in the Jonah Field. As part of this experiment, six explosive charges were detonated in a treatment well ~138 m from a parallel monitoring well (Fig. 1b). The seismic arrivals caused by the explosives were observed on an array of eleven three-component receivers spaced ~11–12 m apart. For simplicity, the three component records (East, North and vertical) were rotated to align one of the horizontal components with the source receiver plane (radial, transverse and vertical). After rotation, the energy of a compressional wave caused by a perforation shot is detected on the radial and vertical components of the receivers only. For completeness, the processing sequence for hydraulic fracture monitoring is summarized in appendix A.

The observed seismograms are dominated by two seismic arrivals that exhibit significantly different frequency contents (Fig. 2). We also note the presence of a third, weak arrival, that is not analyzed in this study (shots 5 and 6 in Fig. 2c). The first arrival, observed at traveltimes between ~22–33 ms, dominates in the high-frequency portion of the signal (0.1–1 kHz). This contrasts with the second arrival, which is observed at traveltimes between ~50–135 ms and dominates in the low-frequency portion of the seismogram (10–100 Hz). The difference in frequency content between the two arrivals is also clearly observed when comparing their respective spectra (see Fig. 3). In Fig. 3 two time windows with a length of 100 ms are used to select the two different arrivals. Time window 1 selects the primary wave energy on the radial component (compare Fig. 2a) and time window 2 selects the secondary wave energy on both the radial and vertical component (compare Figs 2b and 2c).

The high frequency signal corresponds to the direct compressional wave arrival. It is strongest on the radial component (Fig. 2a), and it is not observed on the transverse component. Assuming an isotropic medium, the observed traveltimes indicate a primary wave velocity of 5.3 ± 0.1 km/s. These velocities are ~1 km/s faster than the average compressional wave velocities measured in a borehole located 470 m away from the hydraulic fracture area (Fig. 2c; well log velocities provided courtesy of Encana). This velocity difference is larger than the variability in the well log velocities. Maxwell *et al.* (2006) observed a traveltime variation with incidence angle for perforation shot records and proposed seismic anisotropy as a possible explanation for the difference between vertical velocities and horizontal perforation shot velocities. We stress that this velocity variability cannot explain the traveltime differences analyzed in this study. Finally, the primary wave velocity can be used to estimate the shear wave velocity, using a Vp/Vs ratio of ~1.7 derived from the borehole measurements. This gives a shear wave velocity of ~3.0 km/s.

The secondary, low frequency arrival is clearest on the vertical component (Fig. 2c) and its absolute traveltimes vary with shot depth. The shallowest shot (shot 6 in Fig. 2) corresponds to the longest traveltimes (~120–135 ms) whereas the deepest shot (shot 1 in Fig. 2) produces the shortest traveltimes (~50–63 ms). From the perspective of the receiver array, we note that the secondary arrivals follow an identical relative moveout curve from one perforation shot to another (i.e., the traveltimes with their mean removed are approximately identical). We further note that the wavelets of the secondary

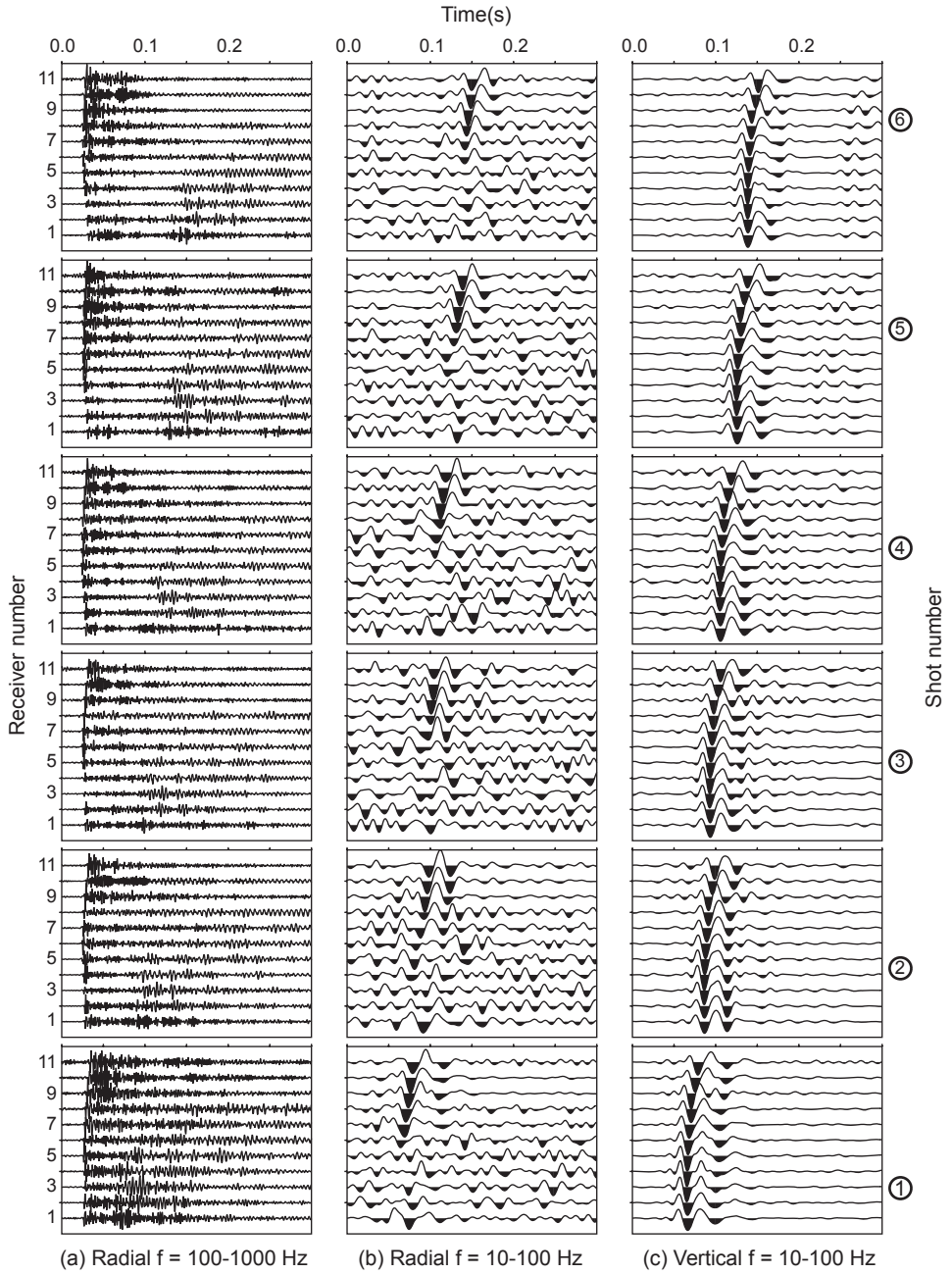

Figure 2 Perforation shot data for one hydraulic fracture stage. The left column (a) shows the high frequency part of the signal observed on the radial receiver, the middle column (b) shows the low frequency signal on the radial receiver and the right column (c) the low frequency signal on the vertical receiver. The top row shows the data for the shallowest perforation shot and the bottom row for the deepest shot. Receiver 1 is the deepest receiver and receiver 11 the shallowest. The radial receiver is horizontal and points towards the treatment well and the vertical receiver points up. The shot numbers mark the depth of the perforation shot relative to the receivers. Comparing the middle and right panels demonstrates the amplitude variation with latitude. While the secondary arrival can be observed on all vertical receivers, it can only be seen on radial receivers with a different elevation from the plug (i.e., receivers 7 to 11).

arrival observed on each receiver are remarkably similar for the different perforation shots. While the secondary arrival is clearly observable on all the vertical components of the receiver array (i.e., from the shallowest to the deepest), it is only observable on the radial components of the shallow receivers (Fig. 2b) and it is not detectable on any of the transverse components.

Comparing the traveltimes of the primary and secondary arrival demonstrates the different nature of the two seismic arrivals. For the primary arrival, the shortest traveltimes are observed at approximately the same depth as the perforation shot, which is to be expected for a direct body wave. In contrast, the shortest traveltimes for the secondary arrival are always detected at the bottom of the array, which precludes direct shear waves as an explanation for the observed seismic arrival.

2.2 Explanation for the secondary arrival

Having established the existence of a robust secondary arrival in the recordings of perforation shots at the Jonah field, we now attempt to identify this arrival. To do so, we propose to explore a range of possible mechanisms for the secondary arrival.

First, we consider direct body waves and waves interacting with a planar interface below the gas layer. These include direct shear waves (ray 1 in Fig. 1a), reflections/conversions at the interface (PP, PS, SP, or SS; ray 2 in Fig. 1a), and critical refractions at the interface (ray 3 in Fig. 1a). For all these scenarios, we find that the estimated traveltime differences between successive shots are too small to match the observations (see appendix B for details). Note that we can also rule out reflections/refractions from a planar interface above the gas layer (ray 4 in Fig. 1a) because they produce the opposite direction of moveout (i.e., the seismic waves arrive earlier at the top than at the bottom of the monitoring well, which is the opposite of what we observe). Thus, this first set of direct, reflected and refracted waves cannot be the cause of the observed secondary arrival.

Second, we investigate whether the secondary arrival could represent a conical wave or a tube wave in the monitoring or treatment well. This scenario also proves inadequate, as we observe that the moveout across the receiver array for each perforation shot requires unrealistic borehole velocities (see appendix C for details).

Finally, we consider the remaining possibility, which is that the secondary arrival corresponds to a tube wave that is diffracted within the treatment well (ray A in Fig. 1a). The ray path corresponding to the calculated traveltimes consists of a segment within the treatment well (shot to plug) with length l_t and a segment through the medium (plug to receiver) with length l_m. Assuming a uniform velocity medium for both the well and the surrounding medium, the traveltime T_d of this diffracted wave can be calculated using the following equation:

$$T_d = v^{-1} l_t + w^{-1} l_m \,, \tag{1}$$

for known (or estimated) values of the body wave velocity w and the tube wave velocity v. The tube wave velocity is unknown. However, for two successive perforation shots the tube wave follows the same trajectory except for the part of the well between the shot locations. We therefore estimate the tube wave velocity by dividing the distance between successive perforation shots by the traveltime difference of seismic arrivals observed on the same receiver. This yields a tube wave velocity estimate of 844 ± 21 m/s. For the second segment we can use the compressional and shear wave velocities derived from the primary wave arrival ($\alpha = 5.3$ km/s and $\beta = 3$ km/s, derived in the last section). Figure 4 shows a comparison between the calculated traveltimes (gray circles) and the observed traveltimes (white squares) for tube waves that are converted to body waves at a borehole plug. We find that only a tube-to-shear-wave conversion gives a satisfactory fit to

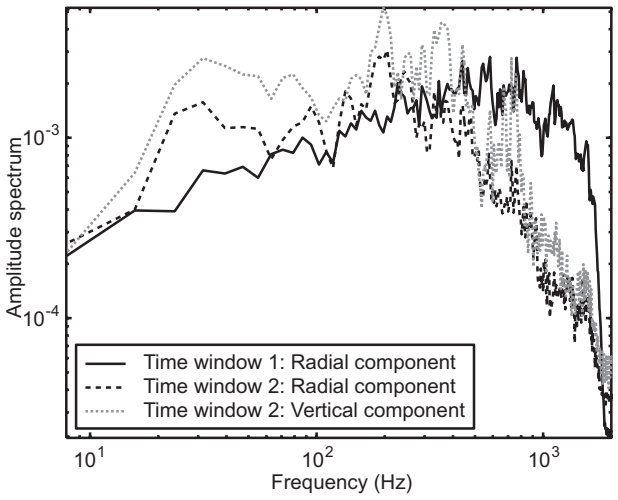

Figure 3 Spectral comparison of the primary and secondary arrivals. The graph shows the amplitude spectra over time windows that isolate the primary arrival (Time window 1) and the secondary arrival (Time window 2), averaged over the 11 receivers located in the monitoring well. Both time windows start 25 ms (0.025s) before the onset of the arrival and last 100 ms (0.1s). The primary arrival has more high frequency and less low frequency energy than the secondary arrival.

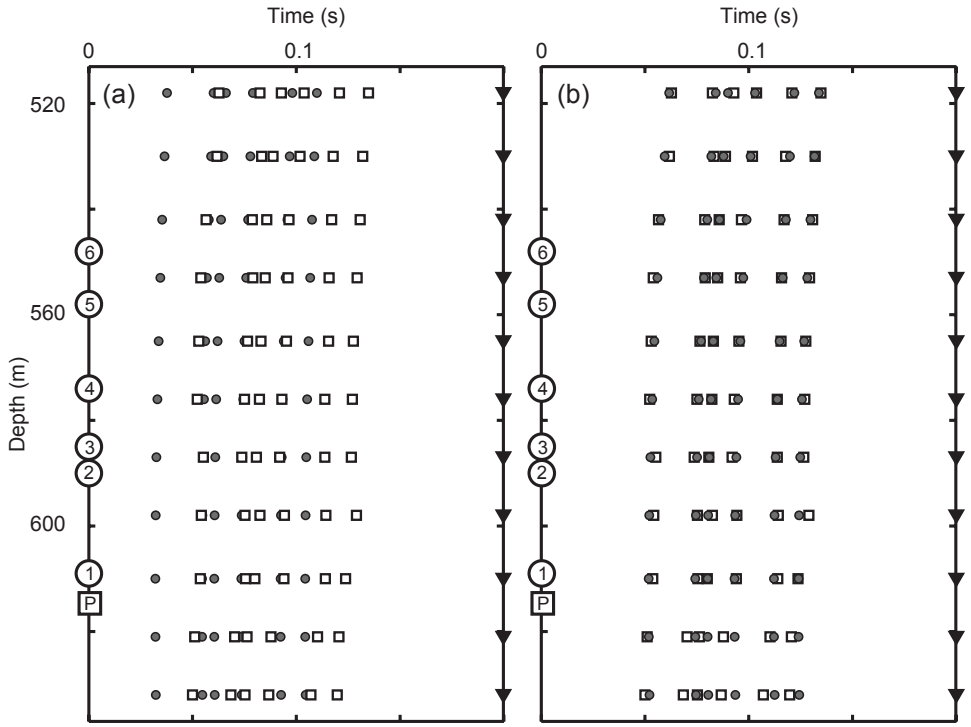

Figure 4 Comparison of observed and estimated arrival times. The large white squares mark the observed secondary arrival times and the gray circles denote the estimated arrival times for tube-to-body-wave conversions diffracted at a plug in the treatment well. For each receiver, the arrival times of the observed secondary wave increase with decreasing shot depth. Panels (a) and (b) show the estimated traveltimes for tube-to-compressional-wave and tube-to-shear-wave conversions, respectively. The numbered circles indicate the shot depth, the square with the letter P denotes the plug depth and the inverted triangles denote the receiver depth

the data (Fig. 4b) and tube-to-compressional-wave conversion does not explain the observations (Fig. 4a).

In the next two sections, we investigate independent observations that lend support to the interpretation of the secondary arrival as a tube-to-shear-wave conversion.

2.3 Moveout and polarization

Our preferred interpretation of the secondary wave requires that the diffracted leg be a shear wave. This requirement can be tested independently by analysing the moveout and polarization of the secondary wave.

The moveout provides an estimate of the velocity of the secondary wave. We start by measuring the slowness separately for each perforation shot by performing a linear regression between the observed secondary wave traveltimes and the plug-receiver distance. For this calculation, we assume that the secondary arrival is diffracted at a borehole plug, but we do not require the tube wave velocity or origin time, because we treat the borehole plug as a secondary source and measure relative arrival times between different receivers. The moveout velocity estimate is then computed by averaging the slowness measurements for the different perforation shots. We evaluate the uncertainty on this estimate by calculating the standard deviation of the measurements. This approach yields a velocity of 2.7 ± 0.4 km/s, which agrees with the shear wave velocity derived above from the primary wave velocity. The velocity uncertainty is most likely caused by lateral velocity variations, raypath curvature, and possibly seismic anisotropy (all of which are not taken into account in our analysis). Despite these velocity uncertainties, we are confident in our interpretation of the signal because the observed traveltime differences cannot be explained through velocity variability alone.

In terms of polarization, a visual inspection of the secondary arrival on the various components of each sensor further confirms that the signal is a vertically polarized shear wave. Indeed, while the secondary arrival is visible on all the receivers for the vertical component (Fig. 2c), it is only visible on the top receivers for the radial component (Fig. 2b). This means that for receivers located at a depth similar to that of the plug (receivers 2&3, Fig. 2), the shear wave travels

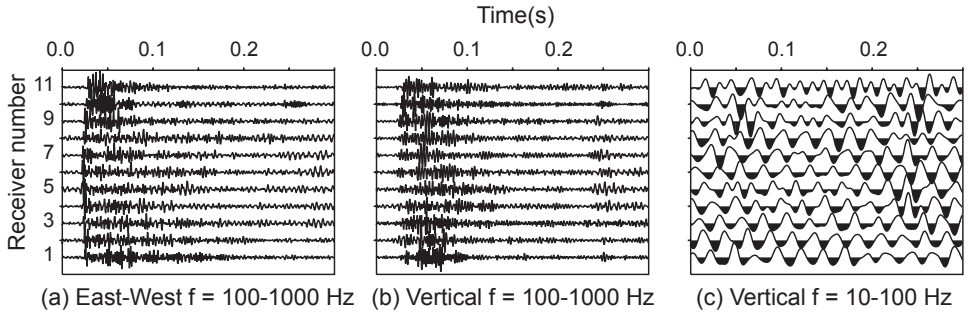

Figure 5 Seismic signals recorded in the monitoring well from a microearthquake located in the immediate vicinity of the treatment well. The records start at the origin time of the microearthquake. The left panel (a) shows the high frequency part of the signal observed on the East-West component. The middle and right panels (b&c) show the high and low frequency part of the signal observed on the vertical receiver. Receiver 1 is the deepest receiver and receiver 11 the shallowest.

almost horizontally and can only be observed on the vertical component. In contrast, for shallow receivers (receivers 7–11, Fig. 2), the ray path has both a vertical and a horizontal component causing a seismic arrival on both the radial and vertical geophone components.

2.4 Microearthquake observations

To further test our interpretation, we compare the perforation shot records with observations from a nearby microearthquake. If the secondary arrival is caused by the interaction between the borehole structure and a tube wave, the secondary arrival should not be observable in the microearthquake record. For this comparison, we selected one microearthquake from a group of microearthquakes that was created by hydraulic fracturing at the treatment well. The microearthquake was selected for its comparatively high signal-to-noise ratio and its proximity to the treatment well (<40 m). By virtue of this proximity, the seismic waves created by the perforation shot and microearthquake follow similar trajectories.

The microearthquake observations confirm our interpretation of the secondary arrival as a tube-to-shear-wave conversion. Indeed, whereas the microearthquake record shows compressional and shear wave arrivals (Fig. 5), it does not generate any observable, low-frequency secondary arrival as that identified in Fig. 2. If the secondary arrival were caused by structure outside the treatment well, this secondary arrival should also be excited by the microearthquake. The absence of the secondary arrival from the microearthquake record implies that its source is located in the borehole and that it is caused by the interaction of tube waves with the borehole structure (most likely a borehole plug).

3 DISCUSSION AND CONCLUSIONS

Perforation shots triggered in a treatment well as part of a hydraulic fracture experiment in the Jonah gas field excite secondary seismic signals that are recorded by geophones in nearby monitoring wells. These signals cannot be explained by direct body (compressional or shear) waves, and they are not observed in recordings of microearthquakes located in the immediate vicinity of the treatment well. Our preferred interpretation is that these secondary signals correspond to tube-to-shear-wave conversions, as these are the only type of waves that can explain the observed traveltimes and amplitudes. While tube-to-compressional-wave conversions might also be expected, they are not clearly visible on the seismograms. The absence of these waves is possibly due to unfavourable acquisition geometry and radiation pattern at the borehole plug.

We identify the borehole wave as a Stoneley wave based on the propagation velocity and frequency content of the signal. Previous investigators have observed tube wave velocities of ~900 m/s in reservoir environments (Hornby and Murphy III 1987; Hardage 2000). The observed tube wave velocity of 844 ± 21 m/s found here is consistent with those results. Furthermore, Cheng and Toksöz (1981) observed that Stoneley waves are the dominant tube wave at low (seismic) frequencies, which is consistent with the properties of the secondary wave we observe.

Interpretation of the frequency content of the secondary arrival is more difficult. In vertical seismic profiles settings, a previous study by Hardage (2000) found that the frequency content of the direct body wave does not necessarily match the frequency of the excited tube wave. This observation is consistent with our observation that the dominant frequency of the primary body wave and secondary tube-to-shear-wave

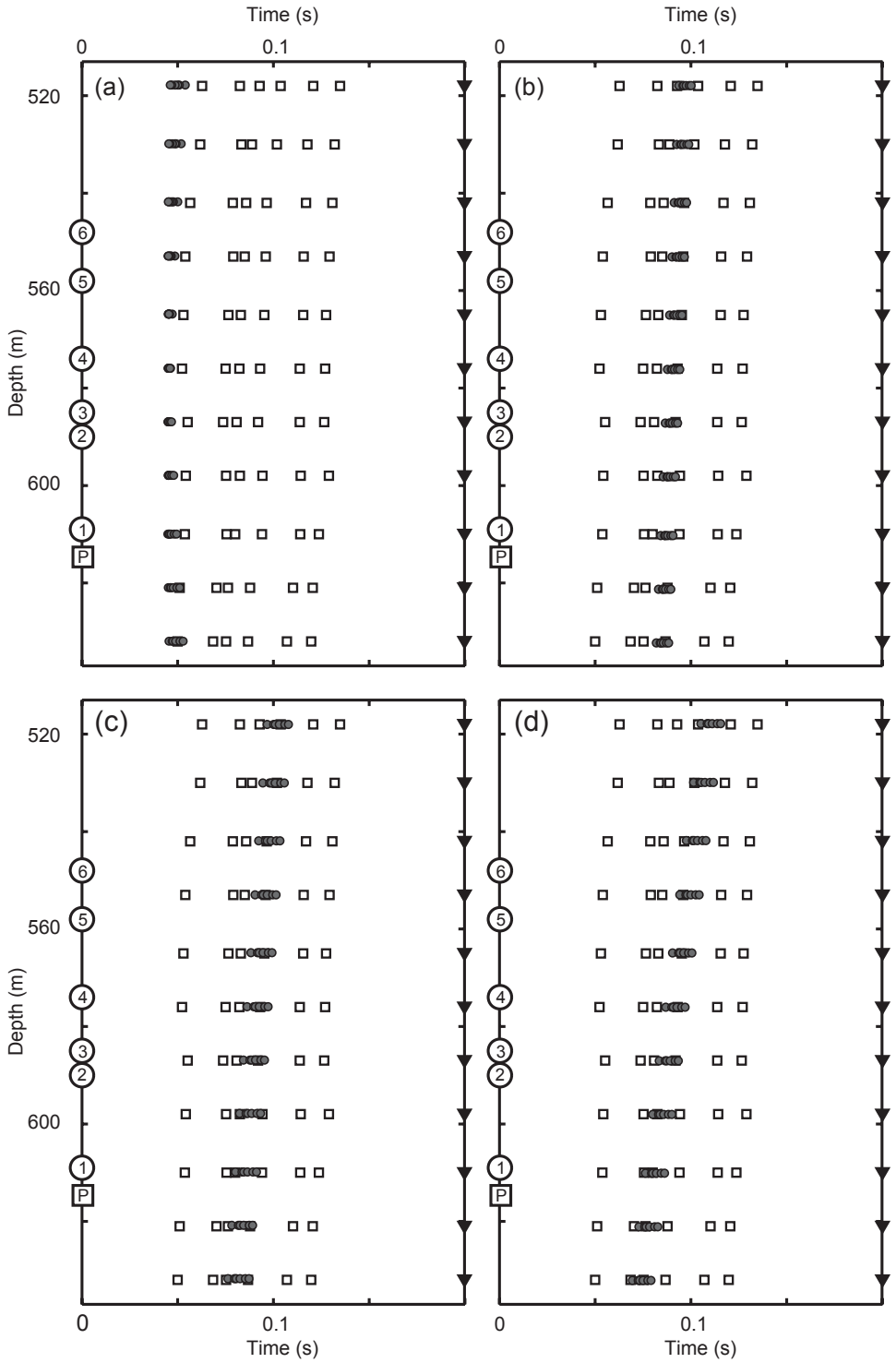

Figure 6 Comparison of observed and estimated traveltimes for the secondary arrival. The white squares mark the secondary arrival times for six perforation shots and the small gray circles the estimated arrival times for (a) direct S-waves, (b) critically refracted P-waves, (c) P-P reflected waves, and (d) P-S reflected waves. For each receiver, the arrival times of the observed secondary wave increase with decreasing shot depth. The numbered circles indicate the shot depth, the square with the letter P the plug depth and the inverted triangles the receiver depth.

conversion differ by an order of magnitude. However, this difference implies that either the perforation shot excites both high frequency body waves and low frequency tube waves, or that tube-to-shear-wave conversion leads to an amplification of low frequencies.

While tube-to-body-wave conversions at discontinuities have been observed before (White and Sengbush 1963; Lee *et al*. 1984), these converted waves have not been systematically explored in the context of hydraulic fracture experiments. The correct identification of these waves is particularly important, because tube-to-shear-wave conversions may easily be confused with direct shear wave arrivals. A distinction between the two is particularly difficult if only a single perforation shot is analyzed. In this study, for example, a direct shear wave would arrive at a similar time as the tube-to-shear-wave conversion generated by the deepest perforation shot (Fig. 6a in the appendix).

Once identified, the converted waves allow the direct, independent measurement of both the tube wave velocity and the formation's shear wave velocity. The tube wave velocity can be estimated from the traveltime difference between two successive perforation shots, provided that the location and time of the perforation shots are known. The formation's shear wave velocity can be calculated based on the moveout of the secondary arrivals across the receiver array for a single perforation shot. This estimate is independent of origin time and tube wave velocity. The latter estimate is particularly useful if the perforation shot did not create observable direct shear waves.

The converted waves identified in this study can help fine-tune the experimental parameters in hydraulic fracturing operations. Better controls on the perforation shots (location and origin time) and the receivers (location, orientation and coupling) yield an improved calibration of the velocity model. This, in turn, allows for a more precise location of induced microseismicity and thereby an improved steering of the hydraulic fracture process. More robust velocity models (including anisotropy) may also help better characterize the fracture direction and stress field in the reservoir.

The observations presented here also have important implications for subsurface velocity estimation and imaging, as they yield improved illumination and increased frequency content. With regards to illumination, the tube-to-body-wave conversions improve the ray coverage because the plug acts as a secondary seismic source that emits waves with different ray paths than those generated by the primary source. This may significantly improve the illumination in obscured parts of the model. With regards to frequency content, it has been shown that the quality of a seismic model is linked to the spectral bandwidth of the available seismic data. For example, Wu and Toksoz (1987) demonstrated that using multiple frequencies improves the image quality in seismic diffraction tomography. Similarly, using low seismic frequencies helps to constrain the long wavelength velocity structure in full waveform inversion (Sirgue and Pratt 2004; Virieux and Operto 2009). However, the spectral bandwidth afforded by active seismic sources is usually limited. In this study, the primary energy of the perforation shots is above 100 Hz while the energy of the secondary arrival is below 100 Hz. Since the frequency contents of the primary and secondary arrivals differ, the secondary arrivals effectively widen the spectrum of available seismic energy and may thus improve the resolution achieved by the recorded seismic waveforms. Integration of the secondary arrivals may therefore help to derive a seismic model or image that is superior to the one derived from primary (direct) arrivals alone.

Finally, our indirect measurements of low-frequency Stoneley wave velocity in the treatment well, in combination with sonic log measurements made at high frequency, may provide a new way to assess velocity dispersion – a property directly related to seismic attenuation. Stoneley waves have been shown to be dispersive in borehole settings. For example, Stewart *et al*. (1984) demonstrated that velocity measurements at sonic and seismic frequencies give significantly different results due to velocity dispersion. Winkler *et al*. (1989) also documented a frequency dependence of Stoneley wave velocities in boreholes. However, to exploit this property for subsurface characterization purposes, one needs to observe low-frequency Stoneley waves. In ideal conditions the tube-to-shear-wave signals identified in this study allow such an observation, and as such they provide a novel means of assessing seismic attenuation near the borehole. This new insight into attenuation, in turn, may yield improved constraints on fracture density, porosity and permeability in the vicinity of the well, which are key parameters for reservoir characterization.

ACKNOWLEDGEMENTS

This work was made possible by funding from MIT's Earth Resources Laboratory and Schlumberger-Doll Research. We would like to thank Julie Shemeta and Nancy House for sharing results and giving us access to Encana's seismic data. We greatly profited from discussions with Mark Willis and Elizabeth LaBarre. We are thankful to two anonymous reviewers and the associate editor, whose advice helped improve our original manuscript.

REFERENCES

Aki K. and Richards P.G. 2002. *Quantitative Seismology*. University Science Books, 2nd edition.

Albright J.N. and Johnson P.A. 1990. Cross-borehole observation of mode conversion from borehole Stoneley waves to channel waves at a coal layer. *Geophysical Prospecting* **38**(6), 607–620.

Aldridge D.F. 1992. Comments on "Conversion points and traveltimes of converted waves in parallel dipping layers" by Gisa Tessmer and Alfred Behle. *Geophysical Prospecting* **40**(1), 101–103.

Aronstam P.S. 2004. Use of minor borehole obstructions as seismic sources. *US Patent* **6**, 747, 914.

Beydoun W.B., Cheng C.H. and Toksöz M.N. 1985. Detection of open fractures with vertical seismic profiling. *Journal of Geophysical Research* **90**(B6), 4557–4566.

Cheng C.H. and Toksöz M.N. 1981. Elastic wave propagation in a fluid-filled borehole and synthetic acoustic logs. *Geophysics* **46**(7), 1042–1053.

Greenhalgh S., Zhou B. and Cao S. 2003. A crosswell seismic experiment for nickel sulphide exploration. *Journal of Applied Geophysics* **53**(2–3), 77–89.

Greenhalgh S.A., Mason I.M. and Sinadinovski C. 2000. In-mine seismic delineation of mineralization and rock structure. *Geophysics* **65**(6), 1908–1919.

Hardage B.A. 2000. *Vertical Seismic Profiling: Principles, vol. 14, Handbook of Geophysical Exploration Seismic Exploration*. Pergamon Press, 3rd edition.

Hornby B.E. and Murphy III W.F. 1987. Vp/Vs in unconsolidated oil sands: Shear from Stoneley. *Geophysics* **52**(4), 502–513.

Kwan A., Dudley J. and Lantz E. 2002. Who really discovered Snell's law? *Physics World* **15**(4), 64.

Lee M.W., Balch A.H. and Parrott K.R. 1984. Radiation from a downhole air gun source. *Geophysics* **49**(1), 27–36.

Maxwell S.C., Shemeta J. and House N. 2006. Integrated anisotropic velocity modeling using perforation shots, passive seismic and vsp data. 68th EAGE Conference & Exhibition, Extended Abstracts, A046.

Norris M. and Aronstam P. 2003. Use of autonomous moveable obstructions as seismic sources. *US Patent* **6**,662,899.

Robinson J.W. and Shanley K.W. (ed.). 2005. *Jonah Field: Case Study of a Tight-Gas Fluvial Reservoir*, Vol. **52**. AAPG Studies in Geology, American Association of Petroleum Geologists and Rocky Mountain Association of Geologists.

Seher T., Rondenay S. and Djikpesse H. 2011. Hydraulic Fracture Monitoring: A Jonah Field Case Study. *Earth Resources Laboratory Consortium Meeting*.

Sirgue L. and Pratt R.G. 2004. Efficient waveform inversion and imaging: A strategy for selecting temporal frequencies. *Geophysics* **69**(1), 231–248.

Stewart R.R., Huddleston P.D. and Kan T.K. 1984. Seismic versus sonic velocities: A vertical seismic profiling study. *Geophysics* **49**(8), 1153–1168.

Taylor G.G. 1989. The point of p-s mode-converted reflection: An exact determination. *Geophysics* **54**(8), 1060–1063.

Tessmer G. and Behle A. 1988. Common reflection point data-stacking technique for converted waves. *Geophysical Prospecting* **36**(7), 671–688.

Tessmer G., Krajewski P., Fertig J. and Behle A. 1990. Processing of PS-reflection data applying a common conversion-point stacking technique. *Geophysical Prospecting* **38**(3), 267–268.

Virieux J. and Operto S. 2009. An overview of full-waveform inversion in exploration geophysics. *Geophysics* **74**(6), WCC1–WCC26.

White J.E. and Sengbush R.L. 1963. Shear waves from explosive sources. *Geophysics* **28**(6), 1001–1019.

Wills P.B., DeMartini D.C., Vinegar H.J., Shlyapobersky J., Deeg W.F., Woerpel J.C., Fix J.E., Sorrelis G.G. and Adair R.G. 1992. Active and passive imaging of hydraulic fractures. *Leading Edge* **11**(7), 15–22.

Winkler K.W., Liu H.-L. and Johnson D.L. 1989. Permeability and borehole Stoneley waves: Comparison between experiment and theory. *Geophysics* **54**(1), 66–75.

Wu R.S. and Toksoz M.N. 1987. Diffraction tomography and multisource holography applied to seismic imaging. *Geophysics* **52**(1), 11–25.

Xu K. and Greenhalgh S. 2010. Ore-body imaging by crosswell seismic waveform inversion: A case study from Kambalda, Western Australia. *Journal of Applied Geophysics* **70**(1), 38–45.

APPENDIX A

Origin time and event location

The origin time of perforation shots and the origin time and location of microseismic events is generally not well known in hydraulic fracturing experiments. When appropriate measurement devices are used, the firing time of perforation shots can be accurately detected through electrical signals that sense the detonator firing. Otherwise, this origin time problem needs to be addressed during data processing. For single receiver wells, a standard workflow usually includes the following processing steps. (1) Waveform data corresponding to the perforation shots are extracted, and used to estimate P-wave and S-wave traveltimes and azimuths. (2) An initial velocity model is derived from well log measurements. (3) The velocity model is updated using the perforation shot traveltimes to account for possible lateral variations. This only requires knowledge of the source and receiver location and allows us to calibrate the origin time of the perforation shot and estimate both P-wave and S-wave velocities. (4) The perforation shot data are used to orient the receivers into a North-South/East-West reference frame. (5) The waveform data corresponding to microearthquakes are extracted and rotated into a North-South / East-West reference frame. P-wave and S-wave traveltimes and azimuths are measured for the microearthquakes. (6) The microearthquakes are relocated using

both traveltime and azimuth data. A more complete description of this workflow and its application to the data from the Jonah field are presented in Seher *et al.* (2011).

APPENDIX B

Traveltimes of direct, reflected and critically refracted waves

The first observation we use to identify the secondary arrival is the traveltime difference between successive shots observed at one receiver (Fig. 2). The variable shot depth is the most likely cause for the traveltime differences, since the explosives perforated the borehole at different depths and all other experiment parameters remained unchanged. To test whether different seismic waves can explain the observed traveltime difference, we calculate traveltimes for direct shear waves, reflections at the base of the formation (PP, PS, SP, or SS), and critical refractions at the base of the formation.

In this study we derive analytic traveltimes for reflections and refractions in a constant velocity medium from Snell's law (Kwan *et al.* 2002). First, we estimate traveltimes for direct shear waves:

$$T_s = \beta_1^{-1}\sqrt{d^2 + (h_s - h_r)^2}\,, \tag{B1}$$

where d stands for the horizontal source receiver spacing, h_s and h_r represent the depth of the source and receiver above the interface, and β_1 denotes the average shear wave velocity of the formation. The traveltime fit is shown in Figure 6a.

Second, we derive analytic traveltimes T_c for critically refracted P waves:

$$T_c = \alpha_1^{-1}(h_s + h_r)\cos\lambda_c + \alpha_2^{-1}d\,, \tag{B2}$$

where α_1 and α_2 denote the velocity in the upper and lower medium, respectively, and λ_c is the critical angle defined by those velocities. To find the depth of the interface and velocity of the lower layer, we minimize the root mean square misfit between the calculated and observed traveltimes using grid search. The best traveltime fit is shown in Fig. 6b.

Third, we estimate analytic traveltimes T_{pp} for compressional wave reflections:

$$T_{pp} = \alpha_1^{-1}\sqrt{d^2 + (h_s + h_r)^2}\,. \tag{B3}$$

We again search the interface depth that provides the smallest root mean square misfit between the observations and the calculated traveltimes. More details can be found in Aki and Richards (2002).

Finally, we evaluate the traveltimes T_{ps} for PS reflections. The traveltimes can be found analytically by solving a quartic equation for the conversion point (Tessmer and Behle 1988; Taylor 1989; Tessmer *et al.* 1990; Aldridge 1992). Instead we evaluate:

$$T_{ps} = \alpha_1^{-1}h_s\sec\lambda_\alpha + \beta_1^{-1}h_r\sec\lambda_\beta\,, \tag{B4}$$

where λ_α and λ_β represent the angles of incidence and reflection of the P- and S-waves, respectively. The angles can be determined from the horizontal slowness $p = \alpha_1^{-1}\sin\lambda_\alpha = \beta_1^{-1}\sin\lambda_\beta$ by solving the equation:

$$\frac{h_s\alpha p}{\sqrt{1-\alpha^2p^2}} + \frac{h_r\beta p}{\sqrt{1-\beta^2p^2}} = d \tag{B5}$$

for the horizontal slowness p. Again, the smallest traveltime misfit is found by varying the depth of the reflecting interface (Fig. 6d). Note that in this analysis we did not consider SS and SP reflections because no direct S waves are observed in the recorded signal.

Each seismic wave can explain some of the observed traveltimes, but none of them explains systematically all the observed traveltimes. In particular, the estimated traveltime differences for any pair of successive shots are always smaller than the observed traveltime differences. Thus, we conclude that direct shear waves and waves reflected/refracted at a bounding horizontal interface do not fit the observed traveltimes. We remark, however, that this analysis demonstrates the need for multiple seismic sources to facilitate the identification of the secondary arrival.

A similar exercise was conducted for reflections/refractions at the top of the formation, but we found that these wave interactions could not explain the secondary arrival either because they produce the wrong moveout (i.e., the seismic waves arrive earlier at the top than at the bottom of the monitoring well, which is the opposite of what we observe).

APPENDIX C

Traveltimes of conical waves and tube waves

The second observation we use to identify the secondary arrival is the traveltime variation for a single shot observed at different receivers (Fig. 2). For the remote observation of conical waves propagating in the treatment well, the total traveltime depends on the traveltime T_t of the wave along the well and the traveltime T_m from the treatment to the monitoring well. The total traveltime T is

$$T \approx T_t + T_m\,. \tag{C1}$$

If the velocity is approximately constant and the two wells are parallel, the traveltime T_m between the treatment

and monitoring well is approximately equal for all receivers. The traveltime difference observed on two receivers is then equal to

$$\Delta T \approx \Delta T_t \approx \Delta l / v \ . \tag{C2}$$

This difference depends on the velocity v inside the treatment well and the path length l along the well. Because the two wells are approximately parallel, this length is approximately equal to the receiver spacing.

This relationship allows us to rule out conical waves in the measurement well as an explanation for the observed secondary arrivals. In this study, we observe a traveltime difference of ~15 ms across the receiver array (Fig. 2). With a receiver array length of 114 m, this would imply a tube wave velocity of ~7.6 km/s – a velocity that is much too high for fluid filled boreholes or the surrounding reservoir.

We note that the same argument rules out a diffraction at the bottom of the monitoring well and the remote observation of tube waves in the treatment well as explanations for the secondary arrival (i.e., both would imply an unrealistically high velocity along the well axis).